

# Path Planning using Neural A\* Search

Ryo Yonetani,<sup>1</sup> Tatsunori Taniyai,<sup>1</sup> Mohammadamin Barekatin<sup>1\*</sup>  
 Mai Nishimura,<sup>1</sup> Asako Kanezaki<sup>2</sup>

<sup>1</sup>OMRON SINIC X    <sup>2</sup>Tokyo Institute of Technology

## Abstract

We present *Neural A\**, a novel data-driven search algorithm for path planning problems. Although data-driven planning has received much attention in recent years, little work has focused on how search-based methods can learn from demonstrations to plan better. In this work, we reformulate a canonical A\* search algorithm to be differentiable and couple it with a convolutional encoder to form an end-to-end trainable neural network planner. *Neural A\** solves a path planning problem by (1) encoding a visual representation of the problem to estimate a movement cost map and (2) performing the A\* search on the cost map to output a solution path. By minimizing the difference between the search results and ground-truth paths in demonstrations, the encoder learns to capture a variety of visual planning cues in input images, such as shapes of dead-end obstacles, bypasses, and shortcuts, which makes estimated cost maps informative. Our extensive experiments confirmed that *Neural A\** (a) outperformed state-of-the-art data-driven planners in terms of the search optimality and efficiency trade-off and (b) predicted realistic pedestrian paths by directly performing a search on raw image inputs.

## Introduction

Path planning refers to the task of finding a valid and low-cost path from start to goal states. Among a variety of path planning algorithms, we are particularly interested in A\* search, a classical search algorithm widely used in many path-planning applications (Smith et al. 2012; Pol and Murugan 2015; Paden et al. 2016). While this fully algorithmic search can surpass human ability in precisely finding optimal solutions for given problems, there is a gap between such approaches and our ability in perceiving problem structures to do planning more intelligently.

As a motivating example, let us start with a simple point-to-point shortest path problem in the grid world in Fig. 1 (a), where the objective is to find a shortest path from the start to the goal nodes (shown as red dots) while avoiding the obstacle (black region). Intuitively, conventional A\* search algorithms discover a solution path by incrementally exploring nodes under the policy to seek a path with the lowest total cost (*i.e.*, path length). However, this approach becomes inefficient when there is an obstacle making a dead-end between the start and the goal, which causes the exploration of

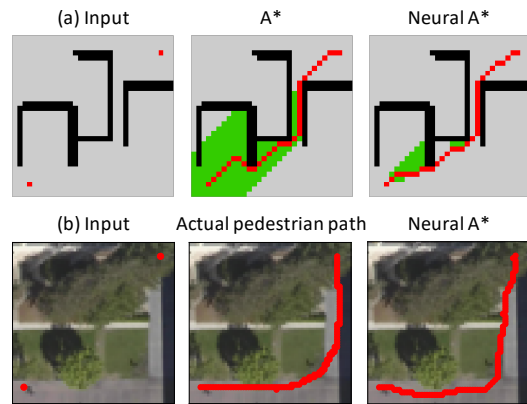


Figure 1: **Path Planning using Neural A\***: (a) Finding a shortest path (red) with fewer node explorations (green). (b) Predicting pedestrian paths (red) on raw image inputs, where passable/impassable regions are not explicitly given.

unnecessarily many nodes that are not a part of the final solution (highlighted in green). In practice, there are a variety of obstacles making the search potentially inefficient. Nevertheless, we as humans can leverage our past experiences to detect such obstacles and find a bypass easily.

Another example that motivates our work is planning on a raw image input of real-world scenes as shown in Fig. 1 (b), where no prior knowledge about the scenes, such as pixel-wise semantic labels (Yuan, Gleason, and Cheriyyadath 2013; Maggiori et al. 2017; Nigam, Huang, and Ramanan 2018), is given. Again, humans can infer from their own experiences which part of the scene is/isn't passable, and can indeed draw efficient paths to their destinations (shown in red). Predicting realistic pedestrian paths while considering implicit scene constraints would be beneficial for practical applications such as assistive navigation (Guerreiro et al. 2019) and evacuation planning (Liu et al. 2018). However, doing so is impossible for vanilla A\* search unless such information about scene structures is provided explicitly.

With these two examples, we argue that one critical feature for path planners is to learn visual representations of planning cues (*i.e.*, *visual planning cues*), such as shapes of dead-end obstacles, bypasses, or shortcuts, from rele-

\*Mohammadamin Barekatin is now at DeepMind.

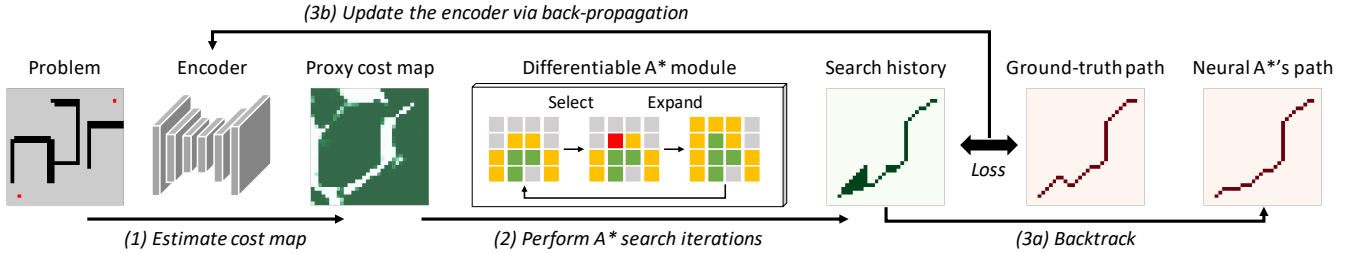


Figure 2: **Schematic Diagram of Neural A\***. (1) Visual representation of a path-planning problem is fed to the encoder to estimate a cost map. (2) Differentiable A\* module performs a point-to-point shortest-path search on the estimated cost map and outputs the search history. (3a) The search history is back-tracked to output a solution path. (3b) During the training phase, the loss between the history and the ground-truth path is back-propagated to update the encoder.

vant planning demonstrations. Acquiring such a learning ability enables conventional A\* search to (a) find solution paths more efficiently and (b) perform path planning directly on raw image inputs without scene structure information. Although much work has been done to develop a variety of data-driven planners (*e.g.*, Tamar et al. (2016); Xiao et al. (2019); Qureshi et al. (2019)), little has focused on how *search-based* planners can benefit from being data-driven. Major technical challenges for data-driven search-based planners include the discrete nature of their path search procedures, which makes it complicated to employ learning via back-propagation. As a solution, Vlastelica et al. (2020) treated a search algorithm as a black-box function and learned visual representations of obstacles via black-box optimization. Although this approach can learn to distinguish obstacles in raw image inputs, it cannot learn to improve the search efficiency since internal search steps are black-boxed. As another relevant attempt, Bhardwaj, Choudhury, and Scherer (2017) proposed a data-driven best-first search method that learned a heuristic function to predict the exact cost from every node to the goal. While this approach can make the search efficient, annotating per-node costs is expensive, cumbersome, and in many cases, not scalable, especially when only raw image inputs are available.

In this paper, we propose a novel data-driven search-based planner named *Neural A\**, with the aim of learning to both improve search efficiency and perform path planning on raw images in a principled fashion. At its core, we reformulate a canonical A\* search algorithm to be differentiable, which we refer to as a differentiable A\* module, by combining a discretized activation technique inspired by Hubara et al. (2016) and linear operations. Doing so enables us to perform the A\* search in the forward pass of neural networks and back-propagate losses through the search procedure to other trainable backbone modules. As illustrated in Fig. 2, Neural A\* consists of a fully-convolutional encoder and the differentiable A\* module, and performs path planning as follows: (1) Given a visual representation of a path planning problem (*i.e.*, map image with start and goal annotations), the encoder estimates a cost map; (2) Differentiable A\* performs a search on the estimated cost map and outputs a search history; (3a) The search history is back-tracked to produce a solution path. To do so, (3b) a loss is computed be-

tween the search history and a ground-truth path and is back-propagated to update the encoder during the training phase. This training allows the encoder to capture visual planning cues in input images and inform the differentiable A\* module where to/not to explore via estimated cost maps.

We extensively evaluate our approach on both simulated and real-world datasets (Sturtevant 2012; Robicquet et al. 2016; Bhardwaj, Choudhury, and Scherer 2017). Our experimental results show that Neural A\* improves the trade-off between search solution’s optimality and efficiency over state-of-the-art data-driven planners (Bhardwaj, Choudhury, and Scherer 2017; Vlastelica et al. 2020) on point-to-point shortest path problems. Moreover, we demonstrate that Neural A\* can learn to predict pedestrian trajectories, given the raw real-world surveillance images.

## Preliminaries

**Path Planning Problem.** Let us consider a path planning problem, in particular a point-to-point shortest path problem, on a graph  $\mathcal{G} = (\mathcal{V}, \mathcal{E})$  where  $\mathcal{V}$  is the set of all nodes representing locations of the world and  $\mathcal{E}$  is the set of potentially valid movements between neighboring locations. For convenience, we define an alternate form  $\mathcal{G} = (\mathcal{V}, \mathcal{N})$  with  $\mathcal{N}(v) = \{v' \mid (v, v') \in \mathcal{E}, v \neq v'\}$  referring to the set of neighbor nodes of  $v$ . Each edge  $(v, v')$  is given a non-negative movement cost  $\phi(v')$  that depends only on the node  $v'$ , where  $\phi(v') = 1$  when  $v'$  is passable and  $\phi(v') = \infty$  otherwise. Given start and goal nodes,  $v_s, v_g \in \mathcal{V}$ , our objective is to find a path consisting of connected nodes,  $P = (v_1, v_2, \dots, v_T) \in \mathcal{V}^T$ ,  $v_1 = v_s$ ,  $v_T = v_g$ , with the total cost  $\sum_{t=1}^{T-1} \phi(v_{t+1})$  (or simply path length  $T - 1$ ) being lowest among all possible paths from  $v_s$  to  $v_g$ . In this work, we exclusively focus on specific yet popular settings where  $\mathcal{G}$  refers to the eight-neighbor grid world.

**A\* Search.** Algorithm 1 overviews the implementation of A\* search we employ in this work. It explores nodes to find a shortest path  $P$  by iteratively (1) selecting a node from the list of candidate nodes that is most promising to construct a shortest path and (2) expanding neighbors of the selected node to update the candidate list, until  $v_g$  is selected.

More specifically, the node selection (Line 3 of Algo-

---

**Algorithm 1** A\* Search

---

**Input:** Graph  $\mathcal{G}$ , moving cost  $\phi$ , start  $v_s$ , and goal  $v_g$

**Output:** Shortest path  $P$

```
1: Initialize  $\mathcal{O} \leftarrow v_s, \mathcal{C} \leftarrow \emptyset, \text{Parent}(v_s) \leftarrow \emptyset$ .
2: while  $v_g \notin \mathcal{C}$  do
3:   Select  $v^* \in \mathcal{O}$  based on Eq. (1).
4:   Update  $\mathcal{O} \leftarrow \mathcal{O} \setminus v^*, \mathcal{C} \leftarrow \mathcal{C} \cup v^*$ .
5:   Extract  $\mathcal{V}_{\text{nbr}} \subset \mathcal{V}$  based on Eq. (2).
6:   for each  $v' \in \mathcal{V}_{\text{nbr}}$  do
7:     Update  $\mathcal{O} \leftarrow \mathcal{O} \cup v', \text{Parent}(v') \leftarrow v^*$ .
8:   end for
9: end while
10:  $P \leftarrow \text{Backtrack}(\text{Parent}, v_g)$ .
```

---

rithm 1) is done based on the following criteria:

$$v^* = \arg \min_{v \in \mathcal{O}} \{g(v) + h(v)\}, \quad (1)$$

where  $\mathcal{O} \subset \mathcal{V}$  is an *open list* that manages candidate nodes for the node selection.  $g(v)$  refers to the actual total cost accumulating  $\phi(v')$  for nodes  $v'$  in a path taken from  $v_s$  to  $v$ , which is updated incrementally during the search. On the other hand,  $h(v)$  is a heuristic function that estimates the total cost from  $v$  to  $v_g$ , where a straight-line distance from  $v$  to  $v_g$  is often used for the grid world. All selected nodes are stored in another list of search histories called *closed list*,  $\mathcal{C} \subseteq \mathcal{V}$ , as done in Line 4.

In Line 5 of Algorithm 1, we expand the neighboring nodes of  $v^*$ ,  $\mathcal{V}_{\text{nbr}} \subset \mathcal{V}$ , based on the following criterion:

$$\mathcal{V}_{\text{nbr}} = \{v' \mid v' \in \mathcal{N}(v^*) \wedge v' \notin \mathcal{O} \wedge v' \notin \mathcal{C}\}. \quad (2)$$

The obtained nodes  $\mathcal{V}_{\text{nbr}}$  are then added to  $\mathcal{O}$  in Line 7 to be selection candidates in the next iteration. The search is terminated once  $v_g$  is selected in Line 3 and stored to  $\mathcal{C}$ , which is followed by `Backtrack` that traces parent nodes  $\text{Parent}(v)$  from  $v_g$  to  $v_s$  to obtain a solution path  $P$ .

**Planning Demonstration.** As introduced in our motivating examples, we consider two cases where (a) passable/impassable locations (*i.e.*,  $\phi$ ) are given explicitly in a given grid world environment or (b) implicitly as raw natural images. For the former case, let  $X \in \{0, 1\}^\Omega$  be a binary image in the fixed 2D space  $\Omega$ , whose element takes 1 for passable locations (*i.e.*,  $\phi(v) = 1$ ) and 0 otherwise. For the latter case where  $\phi$  is not given, let  $X \in [0, 1]^{\Omega \times 3}$  be a color input image. Either way, we refer to a tuple  $D = (X, \mathcal{G}, v_s, v_g, P)$  as a *planning demonstration*.

## Neural A\* Search

Now we present the proposed Neural A\*. As illustrated in Fig. 2, Neural A\* involves a fully-convolutional encoder that takes  $X, v_s, v_g$  as input to capture visual planning cues, such as shapes and locations of dead-end obstacles, bypasses, and shortcuts, in the form of a *proxy* cost map  $\psi(v) \in \mathbb{R}_+$ . High and low costs in  $\psi$  indicate found obstacles and recommended pathways, respectively. Then, the differentiable

A\* module performs the A\* search using  $\psi$ . We aim to learn the Neural A\*, more precisely the encoder, to estimate  $\psi$  from planning demonstrations  $D$  so that:

1. planning with  $\psi$  gives a path close to a ground-truth path  $P$ , *i.e.*, an optimal path when the cost map  $\phi$  is known or a user-demonstrated path planned under unknown  $\phi$ ,
2. fewer nodes are explored compared to when  $\phi$  is used.

In other words, we aim to improve a trade-off between search optimality and efficiency. The former is useful for discovering paths from raw image inputs without explicit annotations about scene structures, while the latter further makes the search efficient. In what follows, we first present the formulation of our differentiable A\* module and then explain how we use it in Neural A\* to train the encoder.

## Differentiable A\* Module

**Variable representations.** We represent variables in Algorithm 1 by a matrix of size  $\Omega$  so that each line can be executed via matrix operations. Specifically, let  $\mathcal{O}, \mathcal{C}, \mathcal{V}_{\text{nbr}} \in \{0, 1\}^\Omega$  be binary matrices respectively indicating nodes contained in  $\mathcal{O}, \mathcal{C}, \mathcal{V}_{\text{nbr}}$ . We describe a start node  $v_s$ , a goal node  $v_g$ , and a selected node  $v^*$  by one-hot indicator matrices,  $V_s, V_g, V^* \in \{0, 1\}^\Omega$  where  $\langle V_s, \mathbf{1}_\Omega \rangle = \langle V_g, \mathbf{1}_\Omega \rangle = \langle V^*, \mathbf{1}_\Omega \rangle = 1$ ,  $\langle A, B \rangle$  is the inner product of two matrices  $A$  and  $B$ , and  $\mathbf{1}_\Omega$  is the all-ones matrix with the size of  $\Omega$ . Moreover, let  $G, H \in \mathbb{R}_+^\Omega$  be a matrix version of  $g(v)$  and  $h(v)$ , and  $\Psi \in \mathbb{R}_+^\Omega$  be a map of proxy costs  $\psi(v)$ .

**Node selection.** Converting Eq. (1) to be differentiable is nontrivial as it involves a discrete operation. To this end, we leverage a discretized activation inspired by Hubara et al. (2016) and reformulate the equation as follows:

$$V^* = \sigma \left( \frac{\exp(-(G+H)/\tau) \odot O}{\langle \exp(-(G+H)/\tau), O \rangle} \right), \quad (3)$$

where  $A \odot B$  denotes the element-wise product and  $\tau$  is a temperature parameter that will be defined empirically.  $\sigma(A)$  is the function that gives the argmax index of  $A$  as a one-hot matrix during a forward pass, while acting as the identity function for back-propagation. The open-list matrix  $O$  is used here to ‘mask’ the exponential term so that the selection is done from the nodes currently in the open list.

**Node expansion.** Expanding neighboring nodes of  $v^*$  in Eq. (2) involves multiple conditions, *i.e.*,  $v' \in \mathcal{N}(v^*)$ ,  $v' \notin \mathcal{O}$ , and  $v' \notin \mathcal{C}$ . Inspired by Tamar et al. (2016), we implement  $\mathcal{N}$  as a convolution between  $V^*$  and the fixed kernel  $K = [[1, 1, 1]^\top, [1, 0, 1]^\top, [1, 1, 1]^\top]$ . When  $X$  is given as a binary image indicating the nodes where  $\phi(v) = 1$ ,  $V_{\text{nbr}}$  is obtained by the following matrix operations.

$$V_{\text{nbr}} = (V^* * K) \odot X \odot (1 - O) \odot (1 - C), \quad (4)$$

where  $A * B$  is the convolution of  $A$  and  $B$ , and  $X, 1 - O$  and  $1 - C$  act as a mask to extract nodes that are passable and not involved in the open nor close lists. When  $X$  is otherwise a natural image that does not explicitly inform the passable nodes, we use  $V_{\text{nbr}} = (V^* * K) \odot (1 - O) \odot (1 - C)$ .

**Updating  $G$ .** As explained earlier,  $g(v)$  is given as the total cost paid for the actual path from  $v_s$  to  $v$ . Here, the value of  $g(v^*)$  for the selected node  $v^*$  can be represented by  $g(v^*) = \langle G, V^* \rangle$ . Then, at each iteration, we partially update actual costs  $G$  for neighbor nodes  $V_{\text{nbr}}$  as follows:

$$G \leftarrow (g(v^*) \cdot \mathbb{1}_\Omega + \Psi) \odot V_{\text{nbr}} + G \odot (1 - V_{\text{nbr}}). \quad (5)$$

Here, the first term computes the new costs of  $V_{\text{nbr}}$  as the current cost of  $v^*$  plus one-step costs  $\Psi$  to its neighbors  $V_{\text{nbr}}$ .

## Training Neural A\*

**Solving multiple problems in a mini-batch.** The complete search algorithm of Neural A\* is summarized in Algorithm 2. To accelerate the training, it is critical to process multiple samples,  $\mathcal{D} = \{D^{(i)} \mid i = 1, \dots, b\}$ , at once in a mini batch of size  $b$  (likewise, we will use the superscript  $i$  to identify variables regarding the  $i$ -th sample in a batch). This is however non-trivial because each sample, *i.e.*, a point-to-point shortest path problem, may be solved with different numbers of iterations. We address this problem by introducing a binary goal verification flag  $\eta^{(i)} = 1 - \langle V_g^{(i)}, V^{*(i)} \rangle$  and update  $O^{(i)}, C^{(i)}$  as follows:

$$O^{(i)} \leftarrow O^{(i)} - \eta^{(i)} V^{*(i)}, \quad C^{(i)} \leftarrow C^{(i)} + \eta^{(i)} V^{*(i)}. \quad (6)$$

Intuitively, this keeps  $O^{(i)}$  and  $C^{(i)}$  unchanged once the goal is found. Then, we repeat Lines 9-15 until we obtain  $\eta^{(i)} = 0$  for all the samples in the batch.

**Loss design.** The output from Neural A\* involves a batch of closed-list matrices  $\mathcal{C} = \{C^{(i)} \mid i = 1, \dots, b\}$ . Here,  $C^{(i)}$  accumulates node selection results based on a proxy cost map  $\Psi^{(i)}$ , *i.e.*, the output of the encoder. We define the L1 loss between  $C^{(i)}$  and  $P^{(i)} \in \{0, 1\}^\Omega$  that represents nodes in a ground-truth path as a binary matrix. By back-propagating the loss through the differentiable A\* module, we can update the encoder to minimize (1) false-negative selection of nodes that should have been taken to find  $P^{(i)}$  and (2) false-positive selection of nodes that were absent in  $P^{(i)}$ . In other words, this training will encourage Neural A\* to (1) search for a path that is close to the ground-truth path (2) with fewer unnecessarily node explorations.

## Experiments

In this section, we first conduct an extensive experiment to evaluate the effect of Neural A\* on the search optimality and efficiency trade-off. Due to space limitations, we present the detail of experimental setups, such as concrete data generation procedures, full implementation details, and the computing infrastructure, in Appendices A and B.

### Datasets

We adopted the following public datasets to collect planning demonstrations with obstacle annotations.

- **Motion Planning Dataset (MP):** A collection of eight types of grid-world environments with unique obstacle shapes (*e.g.*, ‘bugtrap’, ‘forest’) used by Bhardwaj,

---

### Algorithm 2 Neural A\* Search

---

**Input:** Planning demonstrations  $\mathcal{D} = \{D^{(i)} = (X^{(i)}, \mathcal{G}, v_s^{(i)}, v_g^{(i)}, P^{(i)}) \mid i = 1, \dots, b\}$  where  $\mathcal{P} = \{P^{(i)} \mid i = 1, \dots, b\}$  is a set of ground-truth paths.

**Output:** Closed-list matrices  $\mathcal{C} = \{C^{(i)} \mid i = 1, \dots, b\}$  and solution paths  $\mathcal{P}' = \{P'^{(i)} \mid i = 1, \dots, b\}$

- 1: **for all**  $i = 1, \dots, b$  **do in parallel**
  - 2:     Compute  $V_s^{(i)}, V_g^{(i)}$  from  $v_s^{(i)}, v_g^{(i)}$ .
  - 3:     Compute  $\Psi^{(i)}$  from  $X^{(i)}, V_s^{(i)}, V_g^{(i)}$  by the encoder.
  - 4:     Initialize  $O^{(i)} \leftarrow V_s^{(i)}, C^{(i)} \leftarrow 0_\Omega, G^{(i)} \leftarrow 0_\Omega$ .
  - 5:     Initialize  $\text{Parent}^{(i)}(v_s^{(i)}) \leftarrow \emptyset$ .
  - 6:     **end for**
  - 7:     **repeat**
  - 8:         **for all**  $i = 1, \dots, b$  **do in parallel**
  - 9:             Select  $V^{*(i)}$  based on Eq. (3).
  - 10:             Compute  $\eta^{(i)} = 1 - \langle V_g^{(i)}, V^{*(i)} \rangle$ .
  - 11:             Update  $O^{(i)}$  and  $C^{(i)}$  based on Eq. (6).
  - 12:             Compute  $V_{\text{nbr}}^{(i)}$  based on Eq. (4).
  - 13:             Update  $O^{(i)} \leftarrow O^{(i)} + V_{\text{nbr}}^{(i)}$ .
  - 14:             Update  $G^{(i)}$  based on Eq. (5).
  - 15:             Update  $\text{Parent}^{(i)}$  based on Algorithm 1-L6,7.
  - 16:             **end for**
  - 17:     **until**  $\eta^{(i)} = 0$  for  $i = 1, \dots, b$
  - 18:     **if during training then**
  - 19:         Update the encoder by back-propagating the L1 loss between  $\mathcal{C}$  and  $\mathcal{P}$ .
  - 20:     **end if**
  - 21:     **for all**  $i = 1, \dots, b$  **do in parallel**
  - 22:          $P'^{(i)} \leftarrow \text{Backtrack}(\text{Parent}^{(i)}, v_g^{(i)})$ .
  - 23:     **end for**
- 

Choudhury, and Scherer (2017). Each environment consists of 800 training, 100 validation, and 100 test samples, with the same type of obstacles placed in different layouts. We resized each environment map into the size of  $32 \times 32$  to complete the whole experiment in a reasonable time. By following the original setting, training and evaluation were conducted for each environment independently.

- **Tiled Motion Planning Dataset (Tiled MP):** Our extension to the MP dataset to make obstacle structures complex and diverse. Specifically, we tiled four maps drawn randomly from the MP dataset to construct a map with the size of  $64 \times 64$ . We repeated this process to create 3,200 training, 400 validation, and 400 test samples.
- **City/Street Map (CSM):** A collection of 30 city maps with obstacles represented by binary images, provided by Sturtevant (2012). For data augmentation, we cropped multiple random patches with the size of  $128 \times 128$  from each map and resized them to the size of  $64 \times 64$ . We used 20 of the 30 maps to generate random 3,200 training and 400 validation samples and the remaining 10 maps

for 400 test samples. This way we ensured that no maps were shared between training/validation and test splits.

Unlike prior work (Bhardwaj, Choudhury, and Scherer 2017; Vlastelica et al. 2020) that performed evaluations with fixed start and goal locations, we tackled a more challenging setting. Specifically, for each sample, we randomly picked out a single goal location from the four corner regions of the map and one, six, and fifteen start locations from regions sufficiently distant from the goal for training, validation, and test splits, respectively (see Appendix A for more details). We obtained a ground-truth shortest path from each start location to the goal using the Dijkstra algorithm.

## Methods and Implementations

**Neural A\***. As the encoder, we adopted U-Net (Ronneberger, Fischer, and Brox 2015) with the VGG backbone (Simonyan and Zisserman 2015). The concatenation of  $X$  (binary maps representing obstacle layouts) and  $V_s + V_g$  (indicating start and goal locations) was used as an input for the encoder. The final layer was activated by the sigmoid function to constrain proxy cost maps to be  $\Psi \in [0, 1]^\Omega$ . For the differentiable A\* module, the Chebyshev distance was used for the heuristic function  $H$ , where the Euclidean distance multiplied by a small constant (0.001) was further added for the tie-breaking. The temperature  $\tau$  in Eq. (3) was set to the square root of the map width. We also blocked loss gradients from all but  $\Psi$  in Eq. (5) when updating the encoder via back-propagation, as it stabilized the training.

**Baselines.** To show the significance of Neural A\* in terms of the search optimality and efficiency, we adopted the following data-driven search-based planners as baselines.

- **SAIL** (Bhardwaj, Choudhury, and Scherer 2017): A data-driven best-first search method that learns heuristic functions from demonstrations, which resulted in a higher efficiency compared to the standard A\* search and MHA\* (Aine et al. 2016). Unlike Neural A\*, SAIL employs hand-engineered features such as straight distances from each node to the goal and the closest obstacles. We evaluated two variants of SAIL where training samples were rolled out using the estimated heuristic function (**SAIL**) or the ground-truth one (**SAIL-SL**).
- **Blackbox Differentiation** (Vlastelica et al. 2020): A general approach to data-driven combinatorial solvers including search-based path planning. It consists of an encoder module to convert raw-image inputs to cost maps and a solver module that regards a combinatorial solver as a piece-wise constant black-box function taking the cost maps as input. We implemented Blackbox-Differentiation version of Neural A\* (**BB-A\***) that treated our A\* module as a black-box function and trained the encoder via black-box optimization, while keeping other setups, such as an encoder architecture and a loss function, the same with those of Neural A\*.

As another baseline, we evaluated standard best-first search (**BF**) that used the same heuristic function as that of Neural A\* and BB-A\*. Moreover, we implemented a degraded version of Neural A\* named **Neural BF**, which always used

$G = \Psi$  in Eq. (3). By doing so, Neural BF relied solely on the proxy cost of each node without the accumulated one from the start, much like best-first search.

## Experimental Setups

All the models were trained using the RMSProp optimizer, with the mini-batch size, the number of epochs, and the learning rate set to (100, 100, 0.001) for MP dataset and (100, 400, 0.001) for Tiled MP and CSM datasets. Trained models were then evaluated based on the following metrics.

- **Path optimality ratio (Opt)** measuring the number of start locations for each sample, from which a model finds a shortest path in 0 – 100 (%).
- **Reduction ratio of node explorations (Exp)** measuring how much a model can reduce the number of node explorations compared to standard A\* search in 0 – 100 (%). Specifically, by letting  $E^*$  and  $E$  be the number of node explorations by A\* and a model, respectively, it is defined by  $\max(100 \times \frac{E^* - E}{E^*}, 0)$  and averaged over all the start locations for each sample.
- **The Harmonic mean (Hmean)** of Opt and Exp, showing how much their trade-off is improved by a model.

During the training, we saved model weights that marked the best Hmean score on the validation split and used them for measuring final performances on the test split. To investigate statistical differences among models, we computed the bootstrap mean and 95% confidence bounds per metric.

## Results

**Comparisons with baselines.** Table 1 reports quantitative results. Overall, Neural A\* outperformed baseline methods in terms of Opt and Hmean and improved the search optimality and efficiency trade-off. SAIL and SAIL-SL often performed more efficiently, which however came with low optimality ratios especially when maps were getting larger and more complex in the Tiled MP and CSM datasets. BB-A\* demonstrated higher Hmean scores than those of SAIL/SAIL-SL, but was consistently outperformed by Neural A\*. Since BB-A\* and Neural A\* both adopted the identical encoder, the comparison between these two approaches show the importance of making the A\* search differentiable rather than treating it as a black-box function. Interestingly, vanilla best-first search (BF in the table) performed better than SAIL/SAIL-SL in terms of Opt and Hmean. Nonetheless, this would be reasonable because SAIL was originally designed for efficiently finding a feasible path rather than shortest ones. Finally, Neural BF demonstrated the highest Exp in Tiled MP and CSM datasets. However, it was not good at finding optimal paths since it ignored accumulated costs from the start to each node.

**Qualitative results.** Figure 3 visualizes selected search results as well as proxy cost maps learned by Neural A\*. We confirmed higher costs (shown in green) were assigned successfully to the whole obstacle regions creating a dead-end, while lower costs (shown in white) were given to bypasses and shortcuts that efficiently guided the search to the goal.

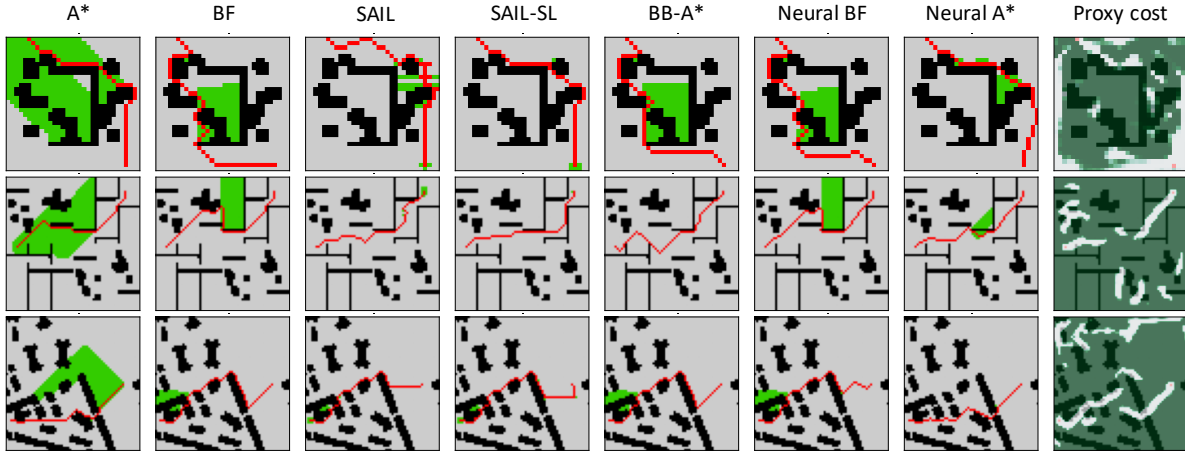


Figure 3: **Selected Path Planning Results.** Black pixels indicate obstacles. Start nodes, goal nodes, and found paths are annotated in red. Explored nodes were highlighted in green. In the most right column, proxy cost maps are overlaid on the input maps where regions with lower costs are visualized in white. More results are presented in Appendix B.

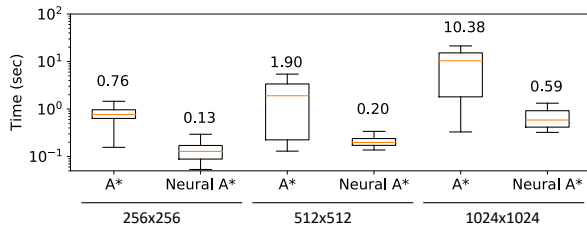


Figure 4: **Results of Planning on Larger Maps:** Boxplots of search runtimes consumed to solve single problems of the sizes  $256 \times 256$ ,  $512 \times 512$ ,  $1024 \times 1024$ .

**Planning on larger maps.** Notably, the encoder of Neural A\* once trained can be combined with other (non-differentiable) A\* search implementations to improve its search runtime for larger maps. To show this, we tiled samples randomly drawn from the MP dataset to create 50 random maps of the sizes  $256 \times 256$ ,  $512 \times 512$ , and  $1024 \times 1024$ . We then measured the runtime to solve a single problem by a standard A\* search implementation when or when not coupled with the encoder trained using Tiled MP dataset of the size  $64 \times 64$ . Although it is not our primary focus to achieve the best possible efficiency, we confirmed that Neural A\* (*i.e.*, A\* coupled with the trained encoder) greatly reduced search runtimes as shown in Fig. 4.

**Limitations.** Although Neural A\* was confirmed to work well on a variety of environments, the current implementation of Neural A\* can be applied only to the grid world environment. Also, similar to other variants of A\* search, our approach is not suitable for problems with a high-dimensional search space. To overcome such limitations, one interesting direction for future work is to extend the proposed approach to planning on general graphs as done by Yang et al. (2020); Xiao et al. (2019) and with a suitable encoder for high-dimensional spaces (Qureshi et al. 2019).

## Path Planning on Raw-Image Inputs

As another application of Neural A\*, we address a task of planning paths directly on raw-image inputs. Specifically, suppose a video of outdoor scenes taken by a stationary surveillance camera. Given planning demonstrations consisting of color images of the scenes and actual trajectories of pedestrians, we aim to learn the Neural A\* so that, given a pair of start and goal locations, it will predict realistic trajectories consistent with those of pedestrians.

**Dataset.** We used Stanford Drone Dataset (SDD) (Robicquet et al. 2016) that comprised surveillance videos captured by static drone cameras at eight distinct locations. We split the dataset in two ways: (1) Intra-scene: collecting one video per location to build a single test split while using the rest to train a model, to see if our approach can predict trajectories of unseen individuals observed in different time; and (2) Inter-scene: performing leave-one-location-out cross-validation to see how learned models can further be generalized for unseen scenes. As planning demonstrations, we extracted pedestrian trajectories and the local patch of a video frame that encompassed the trajectories.

**Implementations.** We compared Neural A\* with BB-A\* that could also plan a path on raw-image inputs. Unlike the previous experiment where obstacle locations were given explicitly, each model now has to learn visual representations of obstacles to avoid them during node selections. Therefore, we modified the U-Net encoder by multiplying the final sigmoid activation by a trainable positive scalar (initialized with 10.0) to impose sufficiently high costs to learned obstacle regions.

**Training setup.** Both of the models were trained using RMSProp with the batch size, the number of epochs, and the learning rate given by (64, 20, 0.001). As an evaluation metric, we used the chamfer distance for assessing dissimilarities between output paths and ground-truth ones.

Table 1: **Quantitative Results:** Bootstrap means and 95% confidence bounds of path optimality ratio (Opt), reduction ratio of node explorations (Exp), and the harmonic mean between Opt and Exp (Hmean).

MP DATASET			
	Opt	Exp	Hmean
BF	65.8 (63.8, 68.0)	44.1 (42.8, 45.5)	44.8 (43.4, 46.3)
SAIL	34.6 (32.1, 37.0)	<b>48.6 (47.2, 50.2)</b>	26.3 (24.6, 28.0)
SAIL-SL	37.2 (34.8, 39.5)	46.3 (44.8, 47.8)	28.3 (26.6, 29.9)
BB-A*	62.7 (60.6, 64.9)	42.0 (40.6, 43.4)	42.1 (40.5, 43.6)
Neural BF	75.5 (73.8, 77.1)	45.9 (44.6, 47.2)	<b>52.0 (50.7, 53.4)</b>
<b>Neural A*</b>	<b>87.7 (86.6, 88.9)</b>	40.1 (38.9, 41.3)	<b>52.0 (50.7, 53.3)</b>
TILED MP DATASET			
	Opt	Exp	Hmean
BF	32.3 (30.0, 34.6)	58.9 (57.1, 60.8)	34.0 (32.1, 36.0)
SAIL	5.7 (4.6, 6.8)	58.0 (56.1, 60.0)	7.7 (6.4, 9.0)
SAIL-SL	3.1 (2.3, 3.8)	57.6 (55.7, 59.6)	4.4 (3.5, 5.3)
BB-A*	31.2 (28.8, 33.5)	52.0 (50.2, 53.9)	31.1 (29.2, 33.0)
Neural BF	43.7 (41.4, 46.1)	<b>61.5 (59.7, 63.3)</b>	44.4 (42.5, 46.2)
<b>Neural A*</b>	<b>63.0 (60.7, 65.2)</b>	55.8 (54.1, 57.5)	<b>54.2 (52.6, 55.8)</b>
CSM DATASET			
	Opt	Exp	Hmean
BF	54.4 (51.8, 57.0)	39.9 (37.6, 42.2)	35.7 (33.9, 37.6)
SAIL	19.6 (17.6, 21.5)	39.6 (37.3, 41.8)	17.0 (15.5, 18.6)
SAIL-SL	12.2 (10.7, 13.7)	38.2 (35.9, 40.5)	12.1 (10.8, 13.4)
BB-A*	54.4 (51.8, 57.1)	40.0 (37.7, 42.3)	35.6 (33.8, 37.4)
Neural BF	60.9 (58.5, 63.3)	<b>42.1 (39.8, 44.3)</b>	40.6 (38.7, 42.6)
<b>Neural A*</b>	<b>73.5 (71.5, 75.5)</b>	37.6 (35.5, 39.7)	<b>43.6 (41.7, 45.5)</b>

Table 2: **Quantitative Results on SDD:** Bootstrap means and 95% confidence bounds of the chamfer distance between predicted and ground-truth pedestrian paths.

	Intra-scene	Inter-scene
BB-A*	178.4 (168.5, 188.0)	138.9 (135.7, 142.0)
<b>Neural A*</b>	<b>30.4 (25.5, 34.6)</b>	<b>47.2 (44.6, 49.7)</b>

**Results.** Table 2 shows that Neural A\* significantly outperformed BB-A\*. As visualized in Fig. 5, Neural A\* predicted paths along roads which were more similar to actual pedestrian trajectories than those by BB-A\* especially under the intra-scene condition. Nevertheless, both approaches sometimes failed to predict actual pedestrian paths when there were multiple possible routes to the destinations, as shown in the example at the bottom. A possible extension to address such problems is to involve a generative framework (Gupta et al. 2018; Salzman et al. 2020) allowing the models to sample multiple paths.

## Related Work

Our work is categorized into data-driven path planning that is aimed at learning from demonstrations to improve its planning ability. It has a variety of applications such as visual navigation (Tamar et al. 2016; Gupta et al. 2017a,b), mobile robot navigation (Kanezaki, Nitta, and Sasaki 2017),

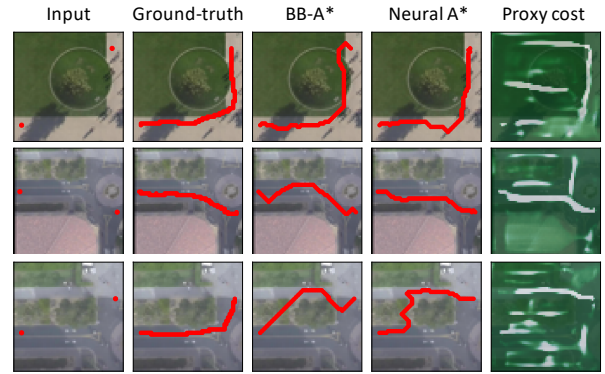


Figure 5: **Path Planning Examples on SDD.** Neural A\* predicted paths similar to actual pedestrian trajectories.

and robot manipulations (Karkus, Hsu, and Lee 2017; Qureshi et al. 2019; Bency, Qureshi, and Yip 2019).

Technically, much work has proposed methods for learning optimal next actions, such as moving left or right, from current states via supervised learning (Tamar et al. 2016; Kanezaki, Nitta, and Sasaki 2017; Gupta et al. 2017a,b; Karkus, Hsu, and Lee 2017; Pérez-Higueras, Caballero, and Merino 2018; Lee et al. 2018; Bency, Qureshi, and Yip 2019) or inverse reinforcement learning (Kim and Pineau 2016; Fu, Luo, and Levine 2018; Yu et al. 2019). While these approaches are beneficial particularly when the environments are dynamic, their reactive planning can sometimes fail to even find a valid path. When the objective is to ensure a high planning success ratio for a given obstacle map, sampling-based planners combined with motion planning networks (Qureshi et al. 2019) could be used.

On the other hand, search-based planning can always find optimal (or near-optimal) paths if performed in static environments, though its data-driven extension has been little studied. As already reviewed in the introduction, the black-box differentiation method was used in (Vlastelica et al. 2020) to execute the Dijkstra algorithm on raw image inputs. Moreover, SAIL (Bhardwaj, Choudhury, and Scherer 2017) was proposed to learn a heuristic function of best-first search. As confirmed in our experiments, however, they were either inefficient or not able to work on raw image inputs with unknown obstacle layouts. By contrast, we present a principled approach to address those two challenges.

## Conclusion

We have presented a novel data-driven search-based planner named Neural A\*, which involves a differentiable A\* algorithm. Neural A\* learns from demonstrations to capture visual planning cues in images, resulting in improving the trade-off between search optimality and efficiency in path planning and also enabling to perform a search directly on raw image inputs. Our extensive experimental evaluations on multiple public datasets have demonstrated the effectiveness of our approach over state-of-the-art planners.

## References

- Aine, S.; Swaminathan, S.; Narayanan, V.; Hwang, V.; and Likhachev, M. 2016. Multi-heuristic A. *The International Journal of Robotics Research* 35(1-3): 224–243.
- Bency, M. J.; Qureshi, A. H.; and Yip, M. C. 2019. Neural path planning: Fixed time, near-optimal path generation via oracle imitation. In *Proceedings of the IEEE/RSJ International Conference on Intelligent Robots and Systems (IROS)*.
- Bhardwaj, M.; Choudhury, S.; and Scherer, S. 2017. Learning heuristic search via imitation. In *Proceedings of the Conference on Robot Learning (CoRL)*.
- Fu, J.; Luo, K.; and Levine, S. 2018. Learning robust rewards with adversarial inverse reinforcement learning. In *Proceedings of the International Conference on Learning Representations (ICLR)*.
- Guerreiro, J.; Ahmetovic, D.; Sato, D.; Kitani, K.; and Asakawa, C. 2019. Airport accessibility and navigation assistance for people with visual impairments. In *Proceedings of the CHI Conference on Human Factors in Computing Systems (CHI)*, 1–14.
- Gupta, A.; Johnson, J.; Fei-Fei, L.; Savarese, S.; and Alahi, A. 2018. Social gan: Socially acceptable trajectories with generative adversarial networks. In *Proceedings of the IEEE Conference on Computer Vision and Pattern Recognition (CVPR)*, 2255–2264.
- Gupta, S.; Davidson, J.; Levine, S.; Sukthankar, R.; and Malik, J. 2017a. Cognitive mapping and planning for visual navigation. In *Proceedings of the IEEE Conference on Computer Vision and Pattern Recognition (CVPR)*, 2616–2625.
- Gupta, S.; Fouhey, D.; Levine, S.; and Malik, J. 2017b. Unifying map and landmark based representations for visual navigation. *arXiv preprint arXiv:1712.08125*.
- Hubara, I.; Courbariaux, M.; Soudry, D.; El-Yaniv, R.; and Bengio, Y. 2016. Binarized neural networks. In *Proceedings of the Advances in Neural Information Processing Systems (NeurIPS)*, 4107–4115.
- Kanezaki, A.; Nitta, J.; and Sasaki, Y. 2017. Goselo: Goal-directed obstacle and self-location map for robot navigation using reactive neural networks. *IEEE Robotics and Automation Letters (RA-L)* 3(2): 696–703.
- Karkus, P.; Hsu, D.; and Lee, W. S. 2017. QMDP-Net: Deep learning for planning under partial observability. In *Proceedings of the Advances in Neural Information Processing Systems (NeurIPS)*, 4694–4704.
- Kim, B.; and Pineau, J. 2016. Socially adaptive path planning in human environments using inverse reinforcement learning. *International Journal of Social Robotics* 8(1): 51–66.
- Lee, L.; Parisotto, E.; Chaplot, D. S.; Xing, E.; and Salakhutdinov, R. 2018. Gated path planning networks. In *Proceedings of the International Conference on Machine Learning (ICML)*.
- Liu, H.; Xu, B.; Lu, D.; and Zhang, G. 2018. A path planning approach for crowd evacuation in buildings based on improved artificial bee colony algorithm. *Applied Soft Computing* 68: 360–376.
- Maggiori, E.; Tarabalka, Y.; Charpiat, G.; and Alliez, P. 2017. Can semantic labeling methods generalize to any city? The Inria aerial image labeling benchmark. In *Proceedings of the IEEE International Geoscience and Remote Sensing Symposium (IGARSS)*.
- Nigam, I.; Huang, C.; and Ramanan, D. 2018. Ensemble knowledge transfer for semantic segmentation. In *Proceedings of the IEEE Winter Conference on Applications of Computer Vision (WACV)*, 1499–1508.
- Paden, B.; Čáp, M.; Yong, S. Z.; Yershov, D.; and Frazzoli, E. 2016. A survey of motion planning and control techniques for self-driving urban vehicles. *IEEE Transactions on Intelligent Vehicles* 1(1): 33–55.
- Paszke, A.; Gross, S.; Massa, F.; Lerer, A.; Bradbury, J.; Chanan, G.; Killeen, T.; Lin, Z.; Gimelshein, N.; Antiga, L.; Desmaison, A.; Kopf, A.; Yang, E.; DeVito, Z.; Raison, M.; Tejani, A.; Chilamkurthy, S.; Steiner, B.; Fang, L.; Bai, J.; and Chintala, S. 2019. PyTorch: An Imperative Style, High-Performance Deep Learning Library. In *Proceedings of the Advances in Neural Information Processing Systems (NeurIPS)*, 8024–8035.
- Pérez-Higueras, N.; Caballero, F.; and Merino, L. 2018. Learning human-aware path planning with fully convolutional networks. In *Proceedings of the IEEE International Conference on Robotics and Automation (ICRA)*, 1–5.
- Pol, R. S.; and Murugan, M. 2015. A review on indoor human aware autonomous mobile robot navigation through a dynamic environment survey of different path planning algorithm and methods. In *Proceedings of the International Conference on Industrial Instrumentation and Control (ICIC)*, 1339–1344.
- Qureshi, A. H.; Simeonov, A.; Bency, M. J.; and Yip, M. C. 2019. Motion planning networks. In *Proceedings of the IEEE International Conference on Robotics and Automation (ICRA)*, 2118–2124.
- Robicquet, A.; Sadeghian, A.; Alahi, A.; and Savarese, S. 2016. Learning social etiquette: Human trajectory understanding in crowded scenes. In *Proceedings of the European Conference on Computer Vision (ECCV)*, 549–565.
- Ronneberger, O.; Fischer, P.; and Brox, T. 2015. U-net: Convolutional networks for biomedical image segmentation. In *Proceedings of the International Conference on Medical Image Computing and Computer Assisted Intervention (MICCAI)*, 234–241.
- Salzmann, T.; Ivanovic, B.; Chakravarty, P.; and Pavone, M. 2020. Trajectron++: Multi-agent generative trajectory forecasting with heterogeneous data for control. In *Proceedings of the European Conference on Computer Vision (ECCV)*.
- Simonyan, K.; and Zisserman, A. 2015. Very deep convolutional networks for large-scale image recognition. In *Proceedings of the International Conference on Learning Representations (ICLR)*.

Smith, C.; Karayiannidis, Y.; Nalpantidis, L.; Gratal, X.; Qi, P.; Dimarogonas, D. V.; and Kragic, D. 2012. Dual arm manipulation - A survey. *Robotics and Autonomous Systems* 60(10): 1340–1353.

Sturtevant, N. 2012. Benchmarks for grid-based pathfinding. *IEEE Transactions on Computational Intelligence and AI in Game* 4(2): 144 – 148.

Tamar, A.; Wu, Y.; Thomas, G.; Levine, S.; and Abbeel, P. 2016. Value iteration networks. In *Proceedings of the Advances in Neural Information Processing Systems (NeurIPS)*, 2154–2162.

Tange, O. 2011. GNU Parallel - The Command-Line Power Tool. *login: The USENIX Magazine* 36(1): 42–47. doi: <http://dx.doi.org/10.5281/zenodo.16303>. URL <http://www.gnu.org/s/parallel>.

Vlastelica, M.; Paulus, A.; Musil, V.; Martius, G.; and Rolínek, M. 2020. Differentiation of blackbox combinatorial solvers. In *Proceedings of the International Conference on Learning Representations (ICLR)*.

Xiao, Z.; Wan, H.; Zhuo, H. H.; Lin, J.; and Liu, Y. 2019. Representation learning for classical planning from partially observed traces. *arXiv preprint arXiv:1907.08352*.

Yakubovskiy, P. 2020. Segmentation Models Pytorch. [https://github.com/qubvel/segmentation\\_models.pytorch](https://github.com/qubvel/segmentation_models.pytorch).

Yang, G.; Zhang, A.; Morcos, A. S.; Pineau, J.; Abbeel, P.; and Calandra, R. 2020. Plan2Vec: Unsupervised representation learning by latent plans. *arXiv preprint arXiv:2005.03648*.

Yu, L.; Yu, T.; Finn, C.; and Ermon, S. 2019. Meta-inverse reinforcement learning with probabilistic context variables. In *Proceedings of the Advances in Neural Information Processing Systems (NeurIPS)*, 11772–11783.

Yuan, J.; Gleason, S. S.; and Cheriyyadat, A. M. 2013. Systematic benchmarking of aerial image segmentation. *IEEE Geoscience and Remote Sensing Letters* 10(6): 1527–1531.

## Appendix A: Details of Experimental Setups

### Dataset Creation

Here we present complementary information on how each dataset was created in our experiments. Since our dataset generation process involves randomness, we fixed a random seed in each program to ensure the reproducibility.

**MP/Tiled-MP/CSM datasets.** In the experiments with MP/Tiled-MP/CSM datasets, we randomized start and goal locations to address more challenging settings unlike prior work (Bhardwaj, Choudhury, and Scherer 2017; Vlastelica et al. 2020) that fixed those locations. Specifically, let  $(W, H)$  be the width and height of input maps, which were set to  $(32, 32)$  for MP and  $(64, 64)$  for Tiled MP and CSM datasets. As illustrated in Fig. A1, we first sampled a single goal location from one of the four corners of size  $(W/4, H/4)$ , which was fixed throughout the experiments. Then we performed the Dijkstra algorithm to compute actual costs from every node to the goal, and calculated the

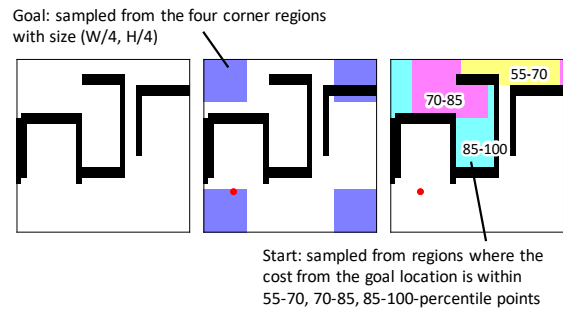


Figure A1: Sampling start and goal locations.

55, 70, 85-percentile points of the costs. For every iteration in the training phase, we sampled a new random start location from regions with the total cost higher than the 55 percentile point. In the validation and testing phases, we sampled two and five random but fixed start locations from each of the regions with the cost within  $[55, 70]$ ,  $[70, 85]$ , and  $[85, 100]$  percentile points. This created  $2 \times 3 = 6$  diverse start locations for the validation and  $5 \times 3 = 15$  for the test splits. Finally, we diluted ground-truth paths with a  $3 \times 3$  kernel when computing the loss for Tiled MP and CSM datasets as it stabilized the training.

**SDD.** In SDD, we extracted some relatively simpler trajectories of pedestrians who moved directly towards their destinations. Specifically, for each single trajectory provided by Robicquet et al. (2016), we first cropped it randomly to have the length in the range of  $[300, 600]$  timesteps (at 2.5fps). Then we calculate the ratio of its straight-line distance between start and goal points to the trajectory length as a measure of path simpleness, which gets lower as trajectories become more complex. We discarded trajectories whose simpleness was less than 0.5. Finally, we cropped image patches so as to encompass each trajectory with the margin of 50 pixels and resized them to the size of  $64 \times 64$ . As a result, 8,325 trajectory samples were extracted from the dataset.

### Hyper-parameter Selection

Table A1 shows the list of hyper-parameters as well as ranges of these values we tried to produce the final results. We selected the final parameters based on the validation performance on MP dataset in terms of Hmean score. As completing all the experiments took a considerably long time (about 80 hours for each baseline/proposed method with a single NVIDIA V100 GPU), we performed each experiment only once with a fixed set of random seeds.

We observed that tie-breaking in A\* search by adding the Euclidean distance from each node  $v$  to the goal scaled by a small positive constant  $(0.001)$  in  $h(v)$ , was critical to improve the base efficiency of A\* search and used this setting throughout all the experiments for all A\*-based methods. The choice of learning rate little affect final performances given a sufficient number of epochs. As for the encoder of Neural A\*, VGG performed better than ResNet (Hmean on MP dataset with VGG: 52.0 / ResNet: 49.2). BB-A\* has an additional hyper-parameter  $\lambda$  that controls the trade-off be-

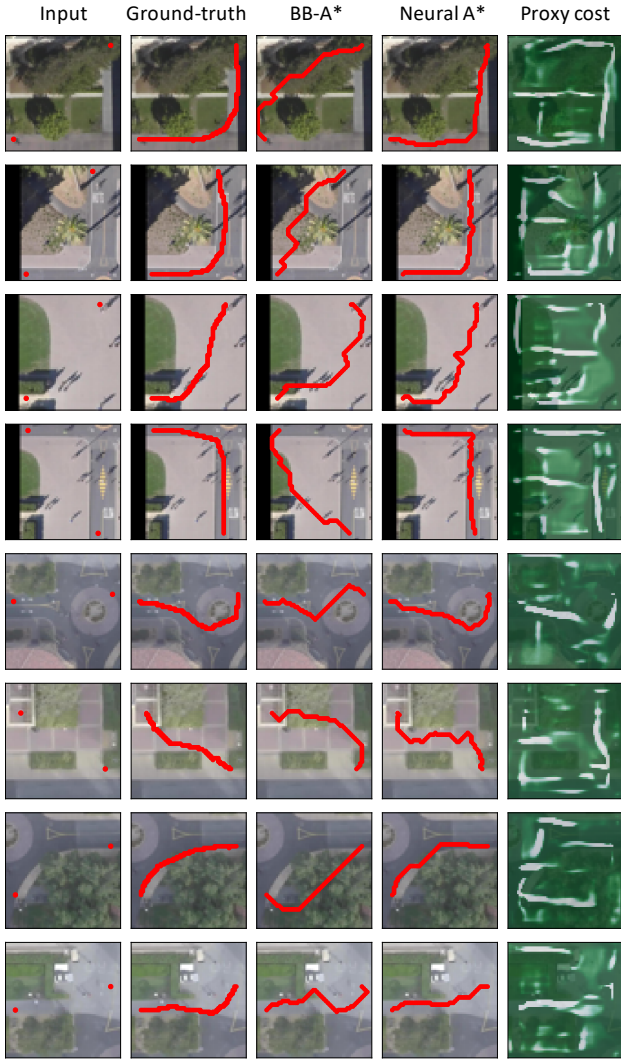


Figure A2: Additional qualitative results (SDD).

tween “informativeness of the gradient” and “faithfulness to the original function” (Vlastelica et al. 2020). We tried several values and found that any choice worked reasonably well except when it was extremely small (*e.g.*, 0.1). Finally, SAIL and SAIL-SL have hyper-parameters on how to collect samples from each training environment instance, which little affected final performances.

### Computing Infrastructure

We performed all the experiments on a server with NVIDIA V100 GPUs, Intel Xeon Gold 6252 CPU @ 2.10GHz (48 cores), and 768GB memory. Our implementation was based on PyTorch 1.5 (Paszke et al. 2019) and Segmentation Models PyTorch (Yakubovskiy 2020), and was executed on Ubuntu 18.04.3 LTS. We used GNU Parallel (Tange 2011) to run multiple experiment sessions in parallel.

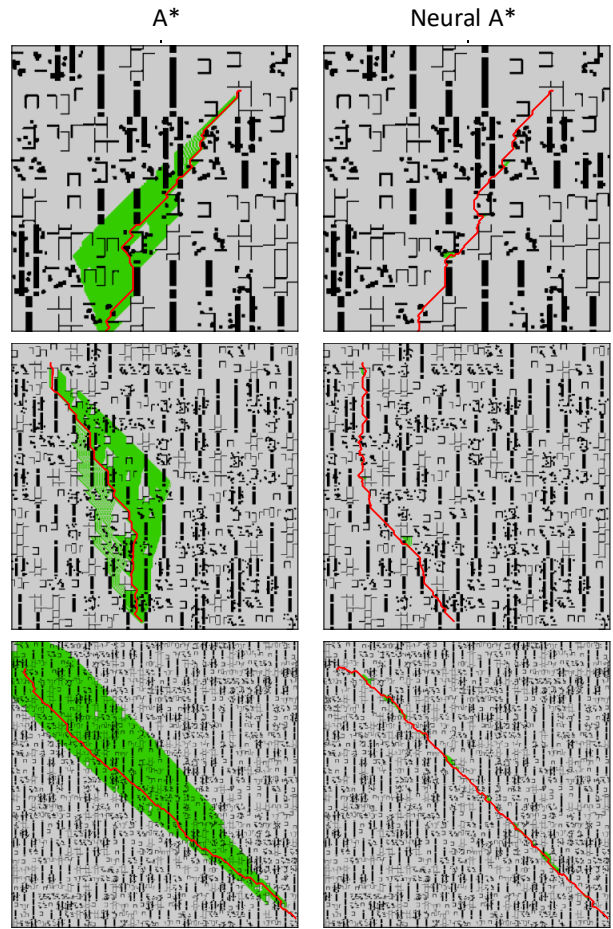


Figure A3: Examples of maps used for measuring search runtimes.

### Details on “Planning for Larger Maps”

In the section “Planning for Larger Maps”, we implemented a python-based A\* search algorithm with `pqdict` package\* for using the priority queue to perform node selections efficiently<sup>†</sup>. In Fig. 4, both A\* and Neural A\* used this A\* search implementation for fair comparisons. To evaluate a search runtime to solve a single problem, we performed the program exclusively on a single CPU core (for performing A\* search) and a single GPU (for running the encoder of Neural A\*), and solved the same problem five times after a single warm-up trial. Neural A\* had additional computational overheads for 1) transferring data between CPU and GPU and 2) performing a single forward pass in the encoder CNN to estimate a proxy cost map. These overheads were however rather negligible compared to the whole runtimes (*e.g.*, around 10% for maps of the size  $256 \times 256$  and less than 1% for those of  $512 \times 512$  and  $1024 \times 1024$ ).

\*<https://github.com/nvictus/priority-queue-dictionary>

<sup>†</sup>Note that other A\* search implementations with different hardware could result in further performance improvements, which is however beyond the scope of this work.

Table A1: List of hyper-parameters and ranges of these values tried during development of the paper.

Parameter Name	Values (range of values tried)
<b>Common</b>	
Optimizer	RMSProp
Learning rate	0.001 (0.0001, 0.0005, 0.001, 0.005)
Batch size	100
Number of epochs	100 (MP), 400 (Tiled MP, CSM)
<b>Neural A*/Neural BF</b>	
Encoder arch	U-Net with VGG backbone (VGG, ResNet)
Temperature $\tau$	$\sqrt{32}$ for MP, $\sqrt{64}$ for Tiled MP and CSM
Tie breaking	$0.001 \times$ Euclidean distance
<b>BB-A*</b>	
Encoder arch	U-Net with VGG backbone
Trade-off parameter $\lambda$	20.0 (0.1, 1.0, 5.0, 10.0, 20.0)
Tie breaking	$0.001 \times$ Euclidean distance
<b>SAIL/SAIL-SL</b>	
Max data samples	300 (60, 300)
Sampling rate	10 (10, 100)
<b>BF</b>	
Tie breaking	$0.001 \times$ Euclidean distance

## Appendix B: Additional Experimental Results

Figures A4 and A2 show additional qualitative results. Moreover, Fig. A3 provides some examples on larger maps used for measuring search runtimes.

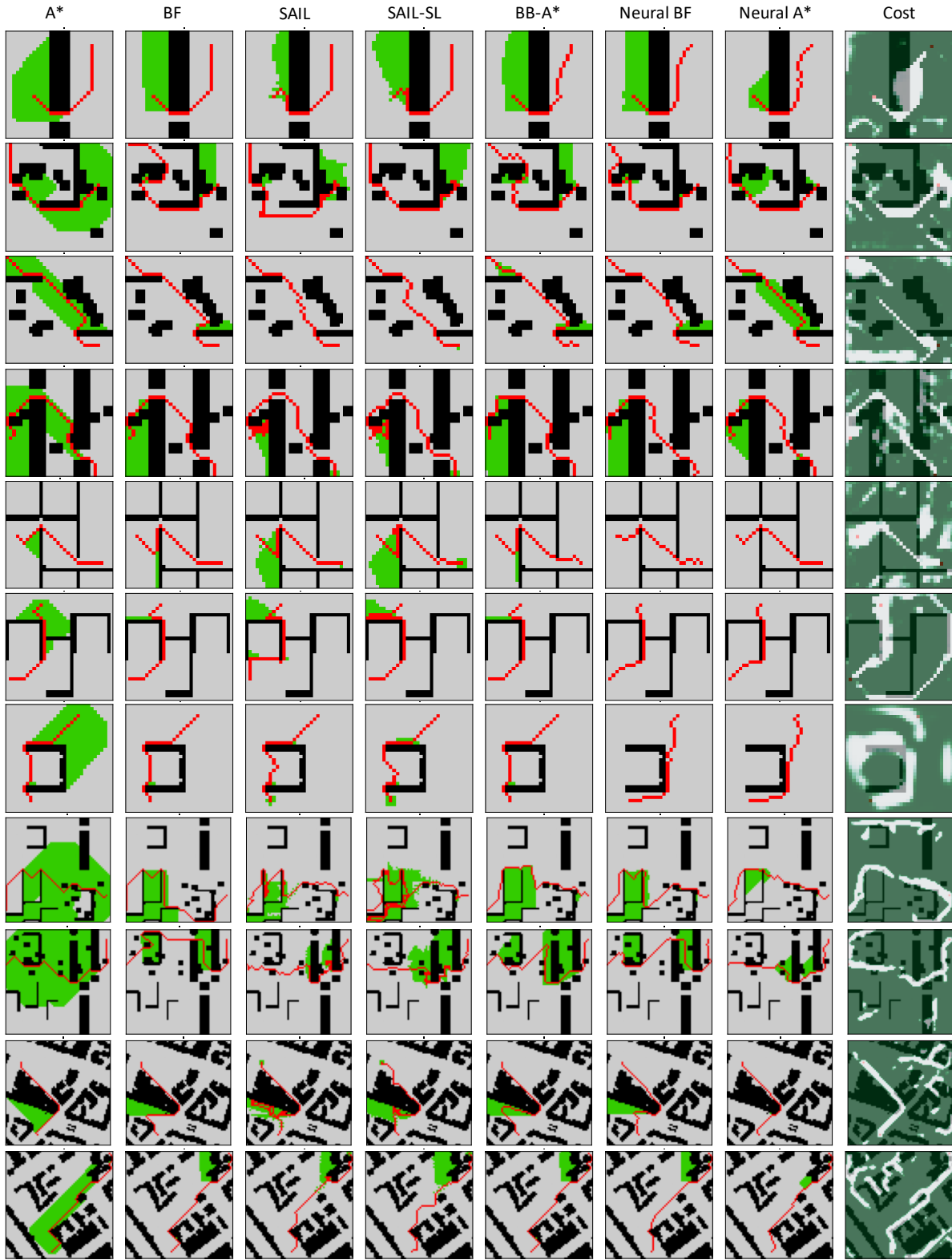


Figure A4: Additional qualitative results (MP/Tiled-MP/CSM Datasets).